

# Spin-Orientation-Dependent Topological States in Two-Dimensional Antiferromagnetic NiTi<sub>2</sub>S<sub>4</sub> Monolayers

Jian Liu,<sup>†,‡</sup> Sheng Meng,<sup>†,‡,§,||</sup> and Jia-Tao Sun<sup>\*,†,⊥</sup>

<sup>†</sup>Beijing National Laboratory of Condensed Matter Physics, and Institute of Physics, Chinese Academy of Sciences, Beijing 100190, P. R. China

<sup>‡</sup>School of Physical Sciences, University of Chinese Academy of Sciences, Beijing 100049, P. R. China

<sup>§</sup>Collaborative Innovation Center of Quantum Matter, Beijing, 100190, P. R. China

<sup>||</sup>Songshan Lake Materials Laboratory, Dongguan, Guangdong 523808, P. R. China

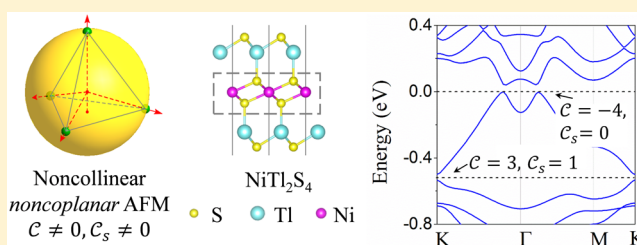
<sup>⊥</sup>School of Information and Electronics, Beijing Institute of Technology, Beijing 100081, P. R. China

**S** Supporting Information

**ABSTRACT:** The topological states of matter arising from the nontrivial magnetic configuration provide a better understanding of physical properties and functionalities of solid materials. Such studies benefit from the active control of spin orientation in any solid, which is known to take place rarely in the two-dimensional (2D) limit. Here we demonstrate by the first-principles calculations that spin-orientation-dependent topological states can appear in the geometrically frustrated monolayer antiferromagnet (AFM).

Different topological states including the quantum anomalous Hall (QAH) effect and time-reversal-symmetry (TRS) broken quantum spin Hall (QSH) effect can be obtained by changing the spin orientation in the NiTi<sub>2</sub>S<sub>4</sub> monolayer. Remarkably, the dilated nc-AFM NiTi<sub>2</sub>S<sub>4</sub> monolayer gives birth to the QAH effect with the hitherto reported largest number of quantized conducting channels (Chern number  $C = -4$ ) in 2D materials. Interestingly, under tunable chemical potential, the nc-AFM NiTi<sub>2</sub>S<sub>4</sub> monolayer hosts a novel state supporting the coexistence of QAH and TRS broken QSH effects with a Chern number of  $C = 3$  and a spin Chern number of  $C_s = 1$ . This work manifests a promising concept and material realization of topological spintronics in 2D antiferromagnets by manipulating their spin degree of freedom.

**KEYWORDS:** Two-dimensional antiferromagnetic material, nontrivial magnetic configuration, quantum anomalous Hall effect, quantum spin Hall effect



Quantum anomalous Hall (QAH) and quantum spin Hall (QSH) effects are conceptually two milestones of topological states, which have attracted enormous research interest in condensed matter physics and material science.<sup>1–10</sup> Both effects benefit from the spin degree of freedom coupled with orbital counterparts, endowing solid materials with great potential in spintronics applications.<sup>11–22</sup> The time-reversal-symmetry (TRS)-broken QAH and TRS-conserved QSH effects manifest the existence of topologically nontrivial states, characterized by the nonzero Chern number  $C$  and odd topological invariant  $\mathcal{Z}_2$ , respectively.<sup>4–6,9,23</sup> Because the Berry curvature is an odd function, the total QAH conductance of the TRS-conserved ( $\Theta$ ) solid materials with a collinear magnetic configuration will vanish. The QSH state consisting of two collinear spin channels of the QAH state is described by topological invariant  $\mathcal{Z}_2 = (C_s^\uparrow - C_s^\downarrow)/2$ , where  $C_s$  is the spin Chern number. In this case,  $\mathcal{Z}_2$  is equivalent to  $|C_s|$ . These novel quantum states of matter originating from the collinear magnetic configuration have laid the foundation of spin-dependent topological states in condensed matter physics.

Recently, spin-orientation-dependent topological states arising from the noncollinear magnetic configuration in geometrically frustrated antiferromagnetic materials have attracted much attention.<sup>24,25</sup> A number of three-dimensional (3D) antiferromagnetic (AFM) materials with noncollinear coplanar magnetic configurations were unexpectedly shown to exhibit a large anomalous Hall effect (AHE) (Figure 1a).<sup>26–30</sup> Furthermore, the noncollinear noncoplanar magnetic configuration of solids can acquire an additional phase proportional to the spin chirality  $S_1 \cdot (S_2 \times S_3)$ , which acts as a fictitious magnetic field yielding the topological Hall effect with a nonzero Chern number of  $C = \pm 1$  (Figure 1b).<sup>31,32</sup> The nonvanishing conductivity in the frustrated antiferromagnets not only conflicts with the conventional wisdom that AHE is proportional to the total net magnetization but also reminds us that novel topological states are related to the complex magnetic configurations therein.<sup>33</sup> The spin-orientation-

**Received:** March 6, 2019

**Revised:** April 24, 2019

**Published:** April 25, 2019

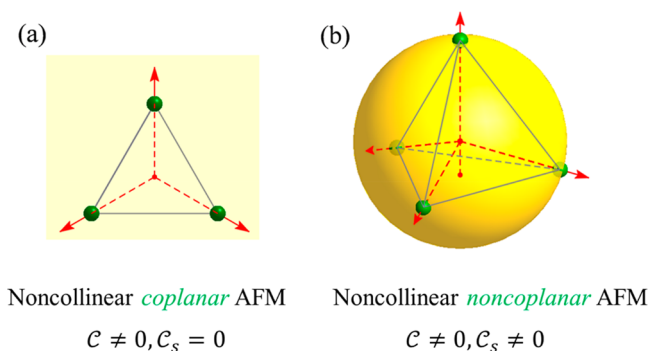


**Figure 1.** Schematics of the spin-orientation-dependent QAH and QSH effect associated with noncollinear coplanar (a) and noncollinear noncoplanar (b) antiferromagnetic state. The Chern number and spin Chern number are denoted by  $C$  and  $C_s$ , respectively.

dependent band structures and topological states arise from strong spin–orbit couplings and large magnetocrystalline anisotropy in bulk antiferromagnetic materials. However, the two-dimensional (2D) antiferromagnetic monolayer has rarely been reported to host spin-orientation-dependent topological states to date.

Here we predict by first-principles calculations that the  $\text{NiTi}_2\text{S}_4$  monolayer as a geometrically frustrated antiferromagnet has spin-orientation-dependent topological states in the 2D limit. We found that the noncollinear noncoplanar AFM (nc-AFM) state is a QAH insulator with a Chern number of  $C = -4$  around the Fermi level, which is significantly different from the state with noncollinear coplanar magnetic configurations. This antiferromagnetic monolayer has the largest

number of quantized conductance channels hitherto found ever to the best of our knowledge. Interestingly, by tuning the chemical potential, a novel topologically nontrivial phase appears that exhibits both QAH and TRS broken QSH phases simultaneously, arising from the complex spin texture in the momentum space.

As shown in Figure 2a,b, bulk  $\text{NiTi}_2\text{S}_4$  crystallizes in a hexagonal lattice with the  $P\bar{3}m1$  space group (No. 164) and is made of structural units of the  $\text{STl-NiS}_2\text{-TlS}$  monolayer stacked along the  $z$  direction with van der Waals (vdW) interlayer separation. The middle  $\text{NiS}_2$  layer (gray box in Figure 2a) has a  $\text{CaCl}_2$ -type structure, and the remaining  $\text{Tl-S}$  part on both sides of  $\text{NiS}_2$  shares the same structural motif with  $\text{GaSe}$ .<sup>34–41</sup> As a candidate of spin liquid material, bulk  $\text{NiTi}_2\text{S}_4$  is one of the members of a large family of triangular lattice antiferromagnet  $\text{NiX}_2\text{Y}_4$  ( $X = \text{Ga, In, Tl}$ ;  $Y = \text{S, Se}$ ) compounds.<sup>34–38</sup> As a result, the  $\text{NiTi}_2\text{S}_4$  monolayer can host a large number of entangled magnetic configurations with coherence beyond the two-spin correlation length at extremely low temperature.<sup>38</sup> Nevertheless, we do not intend to enumerate exhaustively all of the possible magnetic configurations. For the convenience of density functional theory (DFT) calculations, we studied the electronic properties of the  $\text{NiTi}_2\text{S}_4$  monolayer by considering possible magnetic configurations (Supporting Information Figure S2) for up to four sublattices ( $2 \times 2 \times 1$  supercell).<sup>33,42</sup>

We show below that the band structures of the  $\text{NiTi}_2\text{S}_4$  monolayer show a strong dependence on the spin orientation. For example, the t-AFM configuration with a  $120^\circ$  noncollinear coplanar magnetic configuration (inset of Figure 2c) has the lowest total energy with an indirect band gap of 0.24 eV

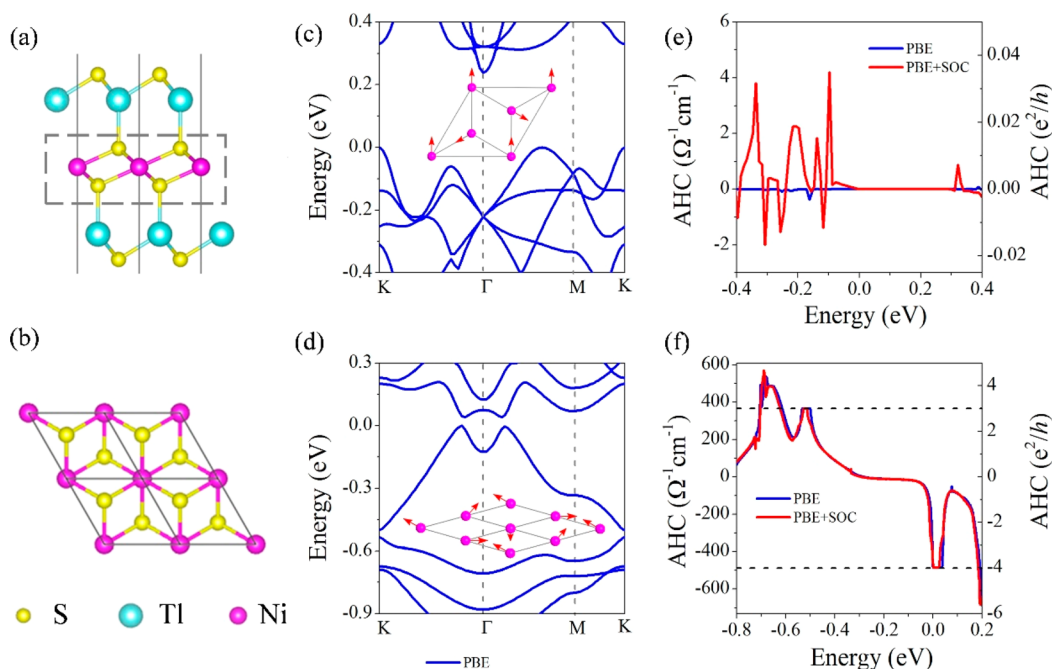


**Figure 2.** Spin-orientation-dependent band structures and anomalous Hall effect of the antiferromagnetic  $\text{NiTi}_2\text{S}_4$  monolayer. (a) Side view of the  $\text{NiTi}_2\text{S}_4$  monolayer. (b) Top view of the middle subunit  $\text{NiS}_2$  shown by the dashed gray line in panel a. (c) Band structure of the noncollinear coplanar antiferromagnetic (t-AFM) state without SOC. The inset is the schematic diagram of t-AFM. (d) Band structure of the 3% diluted nc-AFM  $\text{NiTi}_2\text{S}_4$  monolayer associated with the noncollinear noncoplanar antiferromagnetic state (inset) without considering the SOC. (e) Anomalous Hall conductivity of the t-AFM  $\text{NiTi}_2\text{S}_4$  monolayer without (blue lines) and with (red lines) SOC. (f) Anomalous Hall conductivity of the nc-AFM  $\text{NiTi}_2\text{S}_4$  monolayer without (blue lines) and with (red lines) SOC. The red arrows in c and d represent the spin orientation of each Ni atom (magneta spheres). The Fermi level is shifted at the valence band maximum for the sake of comparison.

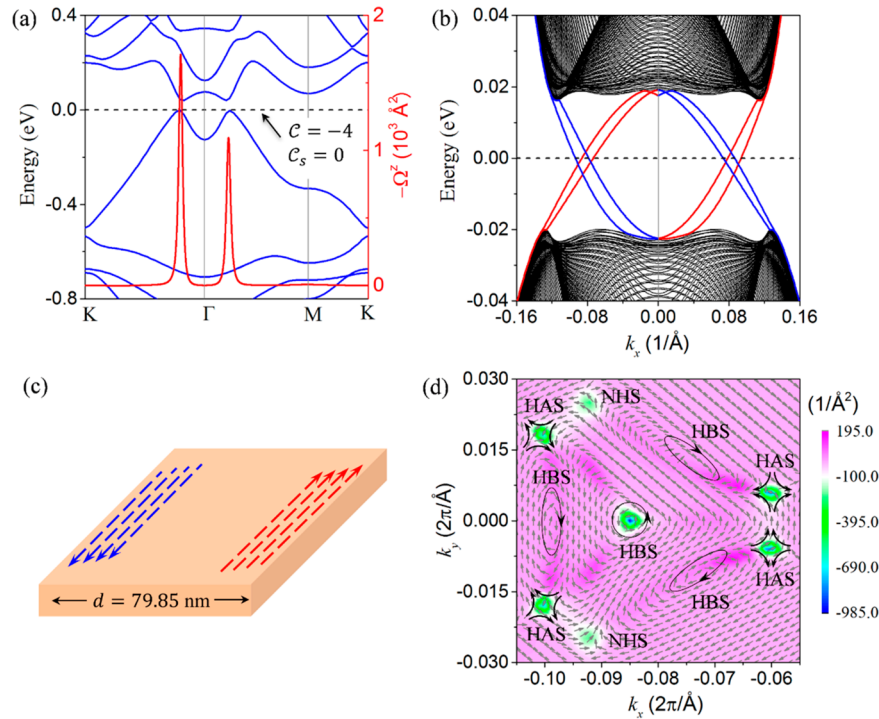


**Figure 3.** Calculated Berry curvature and topologically nontrivial edge states of the nc-AFM NiTi<sub>2</sub>S<sub>4</sub> monolayer. (a) Band structure (blue curves) and the distribution of Berry curvature  $-\Omega^z(k)$  (red curves) along a highly symmetric momentum path. (b) Electronic band structure of the nc-AFM NiTi<sub>2</sub>S<sub>4</sub> nanoribbon with a width of 79.85 nm. (c) Schematics of the propagation direction of spin-opposite edge modes in real space. (d) Spin texture ( $S_x, S_y$ ) for one of two degenerate valence bands around one K valley. The topological charge density has units of  $(1/\text{\AA})^2$ . The length and direction of the gray arrows represent the in-plane component of the normalized spin texture. The black arrows schematically depict the vortex direction. Each blue and magenta region correspond to a half skyrmion, half bloch-skyrmion (HBS), and half antiskyrmion (HAS). NHS denotes the spin texture without forming a half skyrmion.

shown in Figure 2c. In contrast, the nc-AFM NiTi<sub>2</sub>S<sub>4</sub> monolayer with a noncollinear noncoplanar magnetic configuration (inset of Figure 2d) is a semimetal as shown in Figure 2d and Figure S4c, which can be further fully gapped under 3% tensile strain over the whole Brillouin zone as shown in Figure 2d and Figure S5.

Because of the broken time reversal symmetry, it is expected that the NiTi<sub>2</sub>S<sub>4</sub> monolayer in both t-AFM and nc-AFM states has AHE.<sup>43</sup> To this aim, the anomalous Hall conductivity of NiTi<sub>2</sub>S<sub>4</sub> is calculated by using a tight-binding Hamiltonian in maximally localized Wannier functions (MLWF), which is used to fit the first-principles band structures.<sup>44</sup> The Ni *d*, Tl *s*, and S *p* orbitals were used to construct the Wannier Hamiltonian, amounting to 114 and 152 trial atomic orbitals for t-AFM and nc-AFM configurations, respectively. The DFT band structures fitted by the Wannier Hamiltonian are discussed in Figure S10. The transverse Hall conductivity of t-AFM and nc-AFM NiTi<sub>2</sub>S<sub>4</sub> is obtained using the Kubo formula<sup>45,46</sup>

$$\sigma_{xy}(E_f) = -\frac{e^2}{2\pi h} \sum_n \int f(E_f) \Omega^z(k) d^2k \quad (1)$$

where  $f(E_f)$  is the Fermi occupation distribution,  $n$  labels the band number, and  $\Omega_n^z$  denotes the  $z$ -component Berry curvature. The Berry curvature  $\Omega^z$  in eq 1 can be determined from the Kubo formula as

$$\Omega^z(k) = -\sum_{m \neq n} \frac{2\text{Im}\langle \psi_{nk} | \nu_x | \psi_{mk} \rangle \langle \psi_{mk} | \nu_y | \psi_{nk} \rangle}{(E_{mk} - E_{nk})^2} \quad (2)$$

where  $\psi_{nk}$  and  $E_{nk}$  are the Bloch wave function and eigenvalue of the  $n$ th band at the  $k$  point, respectively, and  $\nu_{x(y)}$  is the velocity operator along the  $x(y)$  direction. Specifically, when the Fermi energy  $E_f$  lies inside a gap, the quantized Hall conductivity  $\sigma_{xy}$  is proportional to the Chern number  $C$ , namely,  $\sigma_{xy} = Ce^2/h$ .

As shown in Figure 2e, the calculated anomalous Hall conductivity of t-AFM NiTi<sub>2</sub>S<sub>4</sub> without SOC nearly vanishes, which is qualitatively consistent with those of bulk Mn<sub>3</sub>Ir and Mn<sub>3</sub>Pt.<sup>25,26</sup> After including SOC, the calculated anomalous Hall conductivity of the t-AFM NiTi<sub>2</sub>S<sub>4</sub> monolayer reaches its maximum value of  $4.2 \Omega^{-1} \text{cm}^{-1}$  at  $-0.10$  eV, which can be obtained by hole doping.

We will now show that the nc-AFM configuration has the desired topological nontrivial properties, which is yet found in the t-AFM state. The Mexican-hat-type (MHT) band dispersion (Figure 2d) around the Fermi level is a clear sign of band inversion in the absence of spin-orbit coupling (SOC). We found that the bottom of the conduction band (BCB) mainly originates from *s* orbitals of Tl atoms and *p<sub>z</sub>* orbitals of S atoms, while the top of valence band (TVB) is dominated by (*p<sub>x</sub>*, *p<sub>y</sub>*) orbitals of S atoms and (*d<sub>xz</sub>*, *d<sub>yz</sub>*, *d<sub>xy</sub>*, *d<sub>x<sup>2</sup>-y<sup>2</sup></sub>*) orbitals of Ni atoms as shown in Figures S8 and S9. Because the contribution of *d* orbitals from Ni atoms is comparable to that of *p* orbitals of S atoms, the MHT band dispersion can be viewed as *p*-*pd* band inversion. Besides, it is intriguing that the bands in nc-AFM NiTi<sub>2</sub>S<sub>4</sub> without SOC are all doubly degenerate and the spin for each pair of degenerate bands is in the opposite direction but has the same magnitude below the Fermi level. (The spin eigenvalue in the *x*, *y*, and *z*

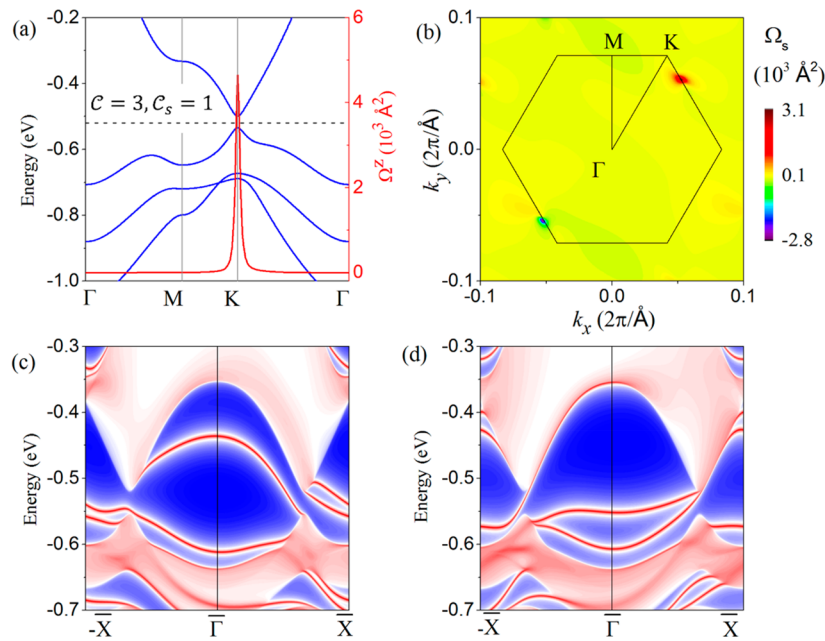


**Figure 4.** Topological states of the 3% dilated nc-AFM NiTi<sub>2</sub>S<sub>4</sub> monolayer when the chemical potential lies near 0.52 eV below the Fermi level. (a) Band structure (blue curves) and the distribution of Berry curvature (red curves) along high-symmetry points. (b) Two-dimensional momentum distribution of spin Berry curvature  $\Omega_s(k)$ . The surface states on the left (c) and right (d) sides of the nc-AFM NiTi<sub>2</sub>S<sub>4</sub> nanoribbon, respectively.

directions as a function of the Fermi level is negligible, as shown in Supporting Information Figure S7.) After the SOC is considered, the two degenerate bands develop a spin splitting without changing the band inversion (Figure 2d and Figure S5b). The momentum-dependent band splitting arising from the SOC is very similar to that of layered K<sub>0.5</sub>RhO<sub>2</sub>.<sup>33</sup>

The calculated Hall conductivity  $\sigma_{xy}$  of the nc-AFM NiTi<sub>2</sub>S<sub>4</sub> monolayer without SOC is displayed as a function of the chemical potential in Figure 2f. We indeed found a clear conductivity plateau with a gap of 37.4 meV around the Fermi level, which is independent of the presence of SOC. The calculated Berry curvature without SOC obtained via eq 2 is plotted in Figure 3a and Figure S11. By integrating the  $\Omega(k)$  of the occupied states over the first Brillouin zone (BZ), the Chern number of the nc-AFM NiTi<sub>2</sub>S<sub>4</sub> monolayer is  $-4$ , in contrast to Chern number  $C = \pm 1$  of systems with spin chirality. As mentioned above, the Chern number corresponds to the quantized conductivity  $\sigma_{xy} = -4e^2/h$ . To the best of our knowledge, this is the hitherto reported largest number of quantized conducting channels in an antiferromagnetic monolayer.

The bulk-boundary correspondence implies that the topological states with nonzero Chern number  $C$  support  $|C|$  branches of chiral gapless modes localized near the edge.<sup>47,48</sup> To further confirm the existence of the topological states, we calculated the energy bands for the nc-AFM NiTi<sub>2</sub>S<sub>4</sub> nanoribbon of  $\sim 80$  nm width (Supporting Information Figure S12) using the tight binding model on the Wannier basis. The calculated band structures of the one-dimensional nanoribbon along the  $b$  axis are shown in Figure 3b. One can clearly observe that there are eight edge conducting channels of opposite chirality within the band inverted gap,<sup>47,48</sup> confirming the quantized nature of topological edge states in the nc-AFM NiTi<sub>2</sub>S<sub>4</sub> monolayer. Figure 3c schematically shows that the four dissipationless conducting channels propagate parallel along the right (left) edge with positive (negative) group velocity. As mentioned above, bulk bands are all doubly

degenerate with their spin exhibiting the opposite direction but the same magnitude. Thus, the edge modes are also doubly degenerate and are spin-opposite.

As mentioned above, the nc-AFM NiTi<sub>2</sub>S<sub>4</sub> has a Chern number of  $C = -4$ , in contrast to the original spin chirality with a Chern number of  $C = \pm 1$ .<sup>33</sup> To illustrate the physical origin of the large number of quantized channels, the momentum distribution of spin textures is studied as shown in Figure 3d. The larger Chern number obtained here stems from the complex spin texture in momentum space (Part VI in Supporting Information). Skyrmion consists of noncollinear spin textures in which the spin quantization axis changes continuously. For two-dimensional systems, the winding number of Skyrmion  $Q = \int_{BZ} q(k_x, k_y) d k_x d k_y$  is a topological charge counting the number of times that a unit spin vector  $\hat{S}(k) = S(k)/|S(k)|$  winds around a unit sphere, where

$$q(k_x, k_y) = \frac{1}{4\pi} (\partial_{k_x} \hat{S} \times \partial_{k_y} \hat{S}) \cdot \hat{S} \quad (3)$$

is the topological charge density in momentum space.<sup>49</sup> We find from the real-spin textures and the topological charge density, as shown in Figure 3d, that each  $K$  valley for one VB consists of five half-skyrmions of  $Q = -\frac{1}{2}$  (representing one half Bloch-skyrmion and four half antiskyrmions) and three half Bloch-skyrmions of  $Q = \frac{1}{2}$ . Thus, the net half skyrmions give rise to a winding number of  $Q = -1$  at each  $K$  valley and a total winding number of  $Q = -2$  for one VB. Considering the fact that the two degenerate VBs are spin-opposite as shown above, their Chern numbers have the same sign and then generating a total Chern number of  $C = -4$ .

Besides the nontrivial gap around the Fermi level, another small gap at  $-0.52$  eV below the Fermi level is shown in Figure 4a. The main contribution of the Berry curvature  $\Omega(k)$  obtained by eq 2 comes from two degenerate valleys  $K$  and  $K'$  (Figure 4a). By integrating the  $\Omega(k)$  over the whole BZ, a

relatively larger Chern number of  $C=3$  is obtained. Because the spatial inversion symmetry of the  $\text{NiTi}_2\text{S}_4$  monolayer is preserved, one may question the existence of the QSH state considering the fact that the bands are all doubly degenerate below the Fermi level. To demonstrate this point, we calculated the spin Berry curvature  $\Omega_s^z(k)$  by replacing the velocity operator  $\hat{v}_x$  with the spin current operator  $\hat{j}_x = \{\hat{v}_x, \hat{s}_z\}$  in eq 2, where  $\hat{s}_z$  is the spin operator.<sup>50–52</sup> The spin Chern number  $C_s$  is obtained in the same way as the Chern number  $C$  as shown before. Figure 4b shows the calculated spin Berry curvature  $\Omega_s^z(k)$  in 2D momentum space. The calculated spin Chern number  $C_s = 1$  indicates that nc-AFM  $\text{NiTi}_2\text{S}_4$  exhibits the time-reversal symmetry-broken QSH effect at  $-0.52$  eV. This state is further verified by the calculated Wannier charge center (WCC) (Figure S13). This is different from the QAH state of nc-AFM  $\text{NiTi}_2\text{S}_4$  with  $C = -4$  and  $C_s = 0$  around the Fermi level. Figure 4c,d shows the corresponding surface states on the left and right surfaces for (010) surface BZ, respectively. The emergence of three topologically protected gapless edge states near  $-0.52$  eV is qualitatively consistent with the quantized Hall conductivity of  $3e^2/h$ .

In conclusion, we have demonstrated that the spin-orientation-dependent topological states are feasible in the two-dimensional antiferromagnetic  $\text{NiTi}_2\text{S}_4$  monolayer. The nc-AFM  $\text{NiTi}_2\text{S}_4$  monolayer exhibits intriguing spin chirality hosting the QAH phase. This state has a very large number of quantized conductance channels with a gap size of 37.4 meV at the Fermi level. Moreover, we reports the first 2D antiferromagnetic monolayer exhibiting both QAH and TRS broken QSH effects  $-0.52$  eV below the Fermi level. As the same family of  $\text{NiTi}_2\text{S}_4$ , the band structures of nc-AFM  $\text{NiX}_2\text{Y}_4$  ( $X = \text{Ga}, \text{In}; Y = \text{S}, \text{Se}$ ) shown in Figure S4 are expectedly very similar to that of  $\text{NiTi}_2\text{S}_4$  around the Fermi level. The above discussion on the spin-orientation-dependent topological states is thus applicable to the same material family. Our work demonstrates that spin orientation could serve as a new degree of freedom of electrons enabling the manipulation of the topological states of two-dimensional magnetic monolayers.

Finally, we comment on the magnetic configuration and the corresponding topological states in monolayer  $\text{NiTi}_2\text{S}_4$  and provide some clues to the experiment feasibility of our prediction. Bulk  $\text{NiGa}_2\text{S}_4$  is a spin liquid material with the number of magnetic configurations depending on the temperature. Previous experiments have confirmed the existence of the noncollinear coplanar AFM configuration in bulk  $\text{NiGa}_2\text{S}_4$ .<sup>38</sup> In principle, the phase transition with different magnetic configurations can be realized by controlling the temperature.<sup>28</sup> As the same family of  $\text{NiGa}_2\text{S}_4$ , however, the electronic structures and magnetic configuration of bulk  $\text{NiTi}_2\text{S}_4$  have never been reported, which is a new system to a certain extent. The topological states with different magnetic configurations in 2D  $\text{NiTi}_2\text{S}_4$  can be measured, in the same way, using the transport experiment as mentioned in bulk  $\text{Mn}_3\text{Pt}$ ,  $\text{Mn}_3\text{Sn}$ , and  $\text{NiGa}_2\text{S}_4$ .<sup>27,38,53,54</sup> The phase transition between different magnetic configurations in 2D  $\text{NiTi}_2\text{S}_4$  can be studied by a transport experiment with exactly controlled temperature.

## ■ ASSOCIATED CONTENT

### Supporting Information

The Supporting Information is available free of charge on the ACS Publications website at DOI: 10.1021/acs.nanolett.9b00948.

Brief description of the methods; magnetic configurations and corresponding electronic structures of the  $\text{NiTi}_2\text{S}_4$  monolayer; fitted band structure by maximally localized Wannier functions; momentum distributions of the spin Berry curvature at different chemical potentials; real spin texture in momentum space; onsite Coulomb interaction  $U$  effect on the topological states (PDF)

## ■ AUTHOR INFORMATION

### Corresponding Author

\*E-mail: jtsun@iphy.ac.cn. Tel: +86-10-82649881.

### ORCID

Sheng Meng: 0000-0002-1553-1432

Jia-Tao Sun: 0000-0003-3519-352X

### Notes

The authors declare no competing financial interest.

## ■ ACKNOWLEDGMENTS

We thank Hongming Weng for fruitful discussions. This work was partially supported by the National Key Research and Development Program of China (2016YFA0202300), the National Natural Science Foundation of China (grant nos. 61725107, 51572290, and 11334006), and the Chinese Academy of Sciences (grant nos. XDB06, XDB30000000, and XDB07030100). Most of the calculations were carried out at the Tianjin Supercomputing Center.

## ■ REFERENCES

- (1) Hu, J.; Zhu, Z.; Wu, R. *Nano Lett.* **2015**, *15*, 2074.
- (2) Qiao, Z.-H.; Ren, W.; Chen, H.; Bellaiche, L.; Zhang, Z.-Y.; MacDonald, A. H.; Niu, Q. *Phys. Rev. Lett.* **2014**, *112*, 116404.
- (3) Qiao, Z.-H.; Yang, S.-Y.; Feng, W.-X.; Tse, W.-K.; Ding, J.; Yao, Y.-G.; Wang, J.; Niu, Q. *Phys. Rev. B: Condens. Matter Mater. Phys.* **2010**, *82*, No. 161414(R).
- (4) Haldane, F. D. *Phys. Rev. Lett.* **1988**, *61*, 2015.
- (5) Ren, Y.-F.; Qiao, Z.-H.; Niu, Q. *Rep. Prog. Phys.* **2016**, *79*, 066501.
- (6) Wan, X.-G.; Turner, A. M.; Vishwanath, A.; Savrasov, S. Y. *Phys. Rev. B: Condens. Matter Mater. Phys.* **2011**, *83*, 205101.
- (7) Liu, H.; Sun, J.-T.; Liu, M.; Meng, S. *J. Phys. Chem. Lett.* **2018**, *9*, 6709.
- (8) Sun, J.-T.; Wang, Z.-F.; Meng, S.; Du, S.-X.; Liu, F.; Gao, H.-J. *2D Mater.* **2016**, *3*, 035026.
- (9) Suzuki, T.; Chisnell, R.; Devarakonda, A.; Liu, Y.-T.; Feng, W.; Xiao, D.; Lynn, J. W.; Checkelsky, J. G. *Nat. Phys.* **2016**, *12*, 1119.
- (10) Liu, H.; Sun, J.-T.; Cheng, C.; Liu, F.; Meng, S. *Phys. Rev. Lett.* **2018**, *120*, 237403.
- (11) Wang, C.; Zhou, X.-Y.; Pan, Y.-H.; Qiao, J.-S.; Kong, X.-H.; Kaun, C.-C.; Ji, W. *Phys. Rev. B: Condens. Matter Mater. Phys.* **2018**, *97*, 245409.
- (12) Burch, K. S.; Mandrus, D.; Park, J. G. *Nature* **2018**, *563*, 47.
- (13) Wu, J.; Liu, J.; Liu, X.-J. *Phys. Rev. Lett.* **2014**, *113*, 136403.
- (14) Qi, X.-L.; Hughes, T. L.; Zhang, S.-C. *Phys. Rev. B: Condens. Matter Mater. Phys.* **2010**, *82*, 184516.
- (15) Zhang, X.; George, T.; Zhang, S.-C.; Isiam, M. S.; Dutta, A. *Proc. SPIE Int. Soc. Opt. Eng.* **2012**, *8373*, 837309.
- (16) Kim, J.; Jhi, S.-H.; MacDonald, A. H.; Wu, R.-Q. *Phys. Rev. B: Condens. Matter Mater. Phys.* **2017**, *96*, No. 140410(R).

- (17) Zhang, H.-B.; Lazo, C.; Blugel, S.; Heinze, S.; Mokrousov, Y. *Phys. Rev. Lett.* **2012**, *108*, 056802.
- (18) Fu, H.-X.; Liu, Z.; Lian, C.; Zhang, J.; Li, H.; Sun, J.-T.; Meng, S. *Phys. Rev. B: Condens. Matter Mater. Phys.* **2016**, *94*, 035427.
- (19) Garrity, K. F.; Vanderbilt, D. *Phys. Rev. Lett.* **2013**, *110*, 116802.
- (20) Chang, C.-Z.; Zhang, J.; Feng, X.; Shen, J.; Zhang, Z.; Guo, M.; Li, K.; Ou, Y.; Wei, P.; Wang, L.-L.; et al. *Science* **2013**, *340*, 167.
- (21) Chang, C. Z.; Zhao, W.; Kim, D. Y.; Zhang, H.; Assaf, B. A.; Heiman, D.; Zhang, S.-C.; Liu, C.; Chan, M. H.; Moodera, J. S. *Nat. Mater.* **2015**, *14*, 473.
- (22) Ezawa, M. *Phys. Lett. A* **2014**, *378*, 1180.
- (23) Zhou, P.; Sun, C.-Q.; Sun, L. Z. *Nano Lett.* **2016**, *16*, 6325.
- (24) Mong, R. S. K.; Essin, A. M.; Moore, J. E. *Phys. Rev. B: Condens. Matter Mater. Phys.* **2010**, *81*, 245209.
- (25) Yang, Y.; Xu, Z.; Sheng, L.; Wang, B.; Xing, D.-Y.; Sheng, D. N. *Phys. Rev. Lett.* **2011**, *107*, 066602.
- (26) Chen, H.; Niu, Q.; MacDonald, A. H. *Phys. Rev. Lett.* **2014**, *112*, 017205.
- (27) Liu, Z. Q.; Chen, H.; Wang, J. M.; Liu, J. H.; Wang, K.; Feng, Z.-X.; Yang, H.; Wang, X.-R.; Jiang, C.-B.; Coey, J. M. D.; Macdonald, A. H. *Nat. Elect.* **2018**, *1*, 172.
- (28) Sürgers, C.; Fischer, G.; Winkel, P.; Löhneysen, H. V. *Nat. Commun.* **2014**, *5*, 3400.
- (29) Nayak, A. K.; Fischer, J. E.; Sun, Y.; Yan, B.; Karel, J.; Komarek, A. C.; Shekhar, C.; Kumar, N.; Schnelle, W.; Kübler, J.; Felser, C.; Parkin, S. S. P. *Sci. Adv.* **2016**, *2*, No. e1501870.
- (30) Kübler, J.; Felser, C. *EPL* **2014**, *108*, 67001.
- (31) Ohgushi, K.; Murakami, S.; Nagaosa, N. *Phys. Rev. B: Condens. Matter Mater. Phys.* **2000**, *62*, R6065.
- (32) Taguchi, Y.; Oohara, Y.; Yoshizawa, H.; Nagaosa, N.; Tokura, Y. *Science* **2001**, *291*, 2573.
- (33) Zhou, J.; Liang, Q.-F.; Weng, H.-M.; Chen, Y.-B.; Yao, S.-H.; Chen, Y.-F.; Dong, J.-M.; Guo, G.-Y. *Phys. Rev. Lett.* **2016**, *116*, 256601.
- (34) Mazin, I. I. *Phys. Rev. B: Condens. Matter Mater. Phys.* **2007**, *76*, 140406.
- (35) Nambu, Y.; Macaluso, R. T.; Higo, T.; Ishida, K.; Nakatsuji, S. *Phys. Rev. B: Condens. Matter Mater. Phys.* **2009**, *79*, 214108.
- (36) Nakatsuji, S.; Tonomura, H.; Onuma, K.; Nambu, Y.; Sakai, O.; Maeno, Y.; Macaluso, R. T.; Chan, J. Y. *Phys. Rev. Lett.* **2007**, *99*, 157203.
- (37) Rushchanskii, K. Z.; Haeuselner, H.; Bercha, D. M. *J. Phys. Chem. Solids* **2002**, *63*, 2019.
- (38) Nakatsuji, S.; Nambu, Y.; Tonomura, H.; Sakai, O.; Jonas, S.; Broholm, C.; Tsunetsugu, H.; Qiu, Y.; Maeno, Y. *Science* **2005**, *309*, 1697.
- (39) Cao, T.; Li, Z.; Louie, S. *Phys. Rev. Lett.* **2015**, *114*, 236602.
- (40) Liu, J.; Hou, W.-J.; Cheng, C.; Fu, H.-X.; Sun, J.-T.; Meng, S. *J. Phys.: Condens. Matter* **2017**, *29*, 255501.
- (41) Cheng, C.; Sun, J.-T.; Chen, X.-R.; Fu, H.-X.; Meng, S. *Nanoscale* **2016**, *8*, 17854.
- (42) Akagi, Y.; Motome, Y. *J. Phys. Soc. Jpn.* **2010**, *79*, 083711.
- (43) Weng, H.-M.; Yu, R.; Hu, X.; Dai, X.; Fang, Z. *Adv. Phys.* **2015**, *64*, 227.
- (44) Mostofi, A. A.; Yates, J. R.; Lee, Y.-S.; Souza, I.; Vanderbilt, D.; Marzari, N. *Comput. Phys. Commun.* **2008**, *178*, 685.
- (45) Yao, Y.; Fang, Z. *Phys. Rev. Lett.* **2005**, *95*, 156601.
- (46) Yao, Y.; Kleinman, L.; MacDonald, A. H.; Sinova, J.; Jungwirth, T.; Wang, D. S.; Wang, E.; Niu, Q. *Phys. Rev. Lett.* **2004**, *92*, 037204.
- (47) Röntynen, J.; Ojanen, T. *Phys. Rev. Lett.* **2015**, *114*, 236803.
- (48) Essin, A. M.; Gurarie, V. *Phys. Rev. B: Condens. Matter Mater. Phys.* **2011**, *84*, 125132.
- (49) Qiao, Z.; Jiang, H.; Li, X.; Yao, Y.; Niu, Q. *Phys. Rev. B: Condens. Matter Mater. Phys.* **2012**, *85*, 115439.
- (50) Rehman, M.; Qiao, Z. *Eur. Phys. J. B* **2018**, *91*, 42.
- (51) Feng, W.-X.; Yao, Y.-G.; Zhu, W.; Zhou, J.; Yao, W.; Xiao, D. *Phys. Rev. B: Condens. Matter Mater. Phys.* **2012**, *86*, 165108.
- (52) Wang, Z.-F.; Su, N. H.; Liu, F. *Nano Lett.* **2013**, *13*, 2842.
- (53) Šmejkal, L.; Mokrousov, Y.; Yan, B.; MacDonald, A. H. *Nat. Phys.* **2018**, *14*, 242.
- (54) Nakatsuji, S.; Kiyohara, N.; Higo, T. *Nature (London, U. K.)* **2015**, *527*, 212.